

Monitoring of cement hydration by broadband time-domain-reflectometry dielectric spectroscopy

N. E. Hager III^{a)}

*Material Sensing & Instrumentation, Inc., Lancaster, Pennsylvania 17601-2212
and Department of Physics and Engineering, Elizabethtown College,
Elizabethtown, Pennsylvania 17022*

R. C. Domszy

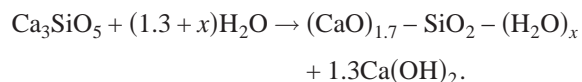
Material Sensing & Instrumentation, Inc., Lancaster, Pennsylvania 17601-2212

(Received 26 April 2004; accepted 31 July 2004)

The broadband complex permittivity is monitored continuously in hydrating cement paste over the frequency range of 10 kHz–8 GHz and from initial mixing to several weeks of cure. Measurements are made by time domain reflectometry (TDR) dielectric spectroscopy, using an adjustable capacitance sensor, which can be embedded in the material *in situ*. The results are fit to a relaxation model, which includes terms representing (1) a Cole-Davidson relaxation near 1 MHz, which grows initially and then decreases with an advancing cure; (2) a Debye relaxation near 100 MHz, which grows initially and then decreases with an advancing cure; (3) a free-water relaxation near 10 GHz, which decreases with an advancing cure; and (4) an ion conductivity and electrode polarization, which decreases with an advancing cure. The model is fit continuously as function of cure time extracting parameters for the relaxation amplitudes, relaxation frequencies, and distribution parameters as a function of cure time. The results are contrasted with measurements in tricalcium silicate and tricalcium silicate with varying ion content, revealing differences that may indicate the nature of the processes involved. Alternative methods for extracting reaction-rate information directly from the TDR transient are presented, providing a robust monitoring procedure usable in the field. Such methods are demonstrated using a variation in temperature and comparison with measurements of reaction heat obtained by calorimetry. © 2004 American Institute of Physics. [DOI: 10.1063/1.1797549]

I. INTRODUCTION

The setting of ordinary portland cement (OPC) is caused by the formation of calcium silicate hydrate (C–S–H) (Ref. 1) by a dissolution-precipitation process² that occurs when calcium silicates react with water. The major component in OPC is tricalcium silicate Ca_3SiO_5 (C_3S), which is often used as a model for studying cement hydration, particularly during the first few days of cure. The hydration reaction for mature C_3S paste is represented as³



The amount of water incorporated in the C–S–H (x) can include chemically bound water ($x=1$ to 2), interlayer or absorbed water, and gel-pore water for pastes cured under saturated conditions.² The ultimate properties of concrete such as compressive strength and pore structure are governed by such hydration reactions, and hence the service life of concrete is largely controlled by cure conditions.

Morphologically, the products of hydration in calcium silicates are classified as high-surface-area outer products formed from the saturated ions in the water-filled pore spaces and low-surface-area inner products formed within the boundaries of the original cement grains.^{2,4} The overall sur-

face area of the hydrating paste increases rapidly during the first 18 h and then levels off, providing evidence that the outer product grows more rapidly at the start of hydration.⁵

Techniques to characterize the nature of bound water in C–S–H include nuclear magnetic resonance (NMR) relaxation measurements,^{2,6} solid-state ^1H NMR experiments,⁷ and quasielastic neutron scattering (QENS).^{8,9} QENS is able to measure the nature of bonded protons and thus the fraction of water that is liquidlike versus the fraction constrained in solid phases.⁹ Three distinct populations of water are identified including free-liquid water, constrained water in the nanoscale gel pores of C–S–H, and chemically bound water. The overall water content and distribution of free, constrained, and bound states is dependent on the age of the paste, the humidity conditions during cure, and the cure temperature. It is suggested that the constrained water is associated solely with the high-surface-area phase of the C–S–H.⁹

A variety of electrical methods can be used to characterize bound-water behavior and cement-paste morphology. At low frequencies, measurements follow dissolved alkali and calcium ions in the nanoporous C–S–H gel, where ion motion in percolative channels creates a dc conductivity, whereas interfacial effects create a low-frequency, polarization. At high frequencies, the water molecule itself is the focus, where the ability of water molecules to reorient in the applied field is dependent on the level of binding. A curing cement paste has water in various states of binding, such as

^{a)}Electronic mail: nehager@msi-sensing.com

physically absorbed water on high-surface-area C–S–H gel pores,¹⁰ chemically bound water associated with silicate layers, and water of crystallization associated with the calcium hydroxide (CH) product. Chemically bound or structural water in C–S–H and CH likely has dielectric properties similar to ice, which has a small loss peak around 100 kHz.¹¹ The dielectric permittivity at high frequencies can thus be used to monitor changes in water chemistry and microstructure during the hydration process.

Though numerous studies have been made investigating the dielectric permittivity at low frequencies, relatively few have been made at high frequencies in the microwave range. Miura *et al.*¹² report complex permittivity measurements at cure times of 1 h and 57 days with multiple relaxations identified in the frequency range of 1 MHz–10 GHz. Measurements are made by time domain reflectometry (TDR) dielectric spectroscopy, using a surface-contact probe attached to preformed samples. Two relaxations are reported around 100 and 1 MHz with the 100-MHz relaxation appearing at 1 h and 1-MHz relaxation appearing at 57 days. Hafine *et al.*¹³ also report complex permittivity measurements at cure times between 10 and 18 h in the range of 1 MHz–1.8 GHz. Measurements are made by reflection methods and the authors report two relaxations occurring around 22 and 1 MHz.

Van Beek¹⁴ reports network analyzer measurements in the range of 1–1000 MHz showing the permittivity at 20 MHz increasing during the first 20 h and then decreasing thereafter. Olp *et al.*¹⁵ show similar results using single-frequency measurements in the range of 1–300 MHz. Ding *et al.*¹⁶ report single-frequency waveguide measurements at 9.5 GHz showing the permittivity decreasing rapidly during the first 5 h and more slowly thereafter. McCarter *et al.*¹⁷ present a complex impedance analysis to 110 MHz, extracting a dc conductivity independent from electrode effects at early cure.

In this paper, we report the continuous monitoring of the complex permittivity of cement paste as a function of cure time over a frequency range of 10 kHz–8 GHz and from the initial mixing to several weeks' cure. We obtain this broad frequency range using TDR dielectric spectroscopy,¹⁸ which follows a 10-GHz frequency response and is not restricted by sweep-oscillator limits. We maintain appropriate impedance over this range using a coaxial pin sensor, which has a capacitance tailored for cement paste and is embedded internally in the material. We capture the full response of this sensor using a long-time nonuniform sampling,¹⁹ which allows access to both low- and high-frequency extremes. Achieving this broad frequency range allows us to better fit a combined relaxation model to the measured frequency spectrum and better resolve the individual model components.

We begin by presenting results for both the complex permittivity and impedance as a function of cure time and by integrating with low-frequency analysis. The results are then fit to a combined relaxation model with terms representing a low relaxation around 1 MHz, a medium relaxation around 100 MHz, and a free relaxation around 20 GHz. The model is fit continuously as a function of cure time in both the real and imaginary components, extracting the evolution of individual model parameters. The results are contrasted with tri-

calcium silicate, the primary component in OPC, and tricalcium silicate with added salt revealing differences that may indicate the nature of the processes involved. We complete the model by extracting single-frequency permittivities as a function of cure time and by comparing with both the broadband and single-frequency measurements in the literature. Lastly, we monitor the hydration rate by following the transient amplitude directly, comparing with variations in temperature and the exothermic heat of reaction.

II. EXPERIMENTAL PROCEDURES

A. Materials

A reference portland cement was obtained from the Cement and Concrete Reference Laboratory (CCRL) at National Institute of Standards and Technology. The material is an American Institute of Standards and Technology Type I ordinary portland cement with a Blaine fineness of 394 m²/kg.²⁰ It contains 0.82 wt % readily soluble K₂O and 0.12 wt % readily soluble Na₂O.²¹ Tricalcium silicate was obtained from the Construction Technology Laboratories Inc.²² The material is made from alite, a “doped” monoclinic form of C₃S, which is chemically similar to C₃S in OPC. Samples are produced by milling and sieving through a 400 US mesh.

Starting powders (20 g) are mixed with distilled water in a water-to-cement (w/c) ratio of 0.4 by weight. An isothermal heat-conduction calorimeter (Themometric Ltd., model Thermal Activity Monitor Air) monitors the heat generated during isothermal cure at 23 °C.

B. TDR background

The expressions governing the TDR dielectric spectroscopy are described in the literature.¹⁸ A voltage pulse $v_o(t)$ propagating along a transmission line of characteristic admittance G_c encounters a terminating capacitance sensor of admittance Y to produce a reflected pulse $r(t)$. The terminating admittance is the total current-to-voltage ratio $G_c(v_o - r)/(v_o + r)$, where v_o and r are the Laplace transforms of the incident and reflected pulses. The terminating admittance is related to the sample permittivity ϵ by $Y = i\omega\epsilon C_o$, so the permittivity is written as

$$\epsilon^*(\omega) = \frac{G_c}{i\omega C_o} \frac{v_o - r}{v_o + r}, \quad (1)$$

where C_o is the geometric capacitance of the empty sensor. To establish a common time reference, the incident voltage is replaced by the empty-sensor reflection, writing Eq. (1) for both the empty-sensor and sample reflections and solving them to eliminate v_o . The result is a reflection coefficient ρ of similar form as

$$\rho^*(\omega) = \frac{G_c}{i\omega C_o} \frac{r_r - r_x}{r_r + r_x}, \quad (2)$$

where r_r and r_x are the Laplace transforms for the empty-sensor and sample reflections. The permittivity is obtained from a differential expression, which corrects the difference

between the incident pulse and empty-sensor reflection at high frequencies,

$$\varepsilon^*(\omega) = \frac{\rho + 1}{1 - (\omega C_o / G_c)^2 \rho}. \quad (3)$$

Equation (3) can be generalized to a bilinear calibration form, where the differential terms are replaced by the frequency-dependent complex parameters, which contain the unknown transmission line characteristics. Equation (3) can then be written as

$$\varepsilon^*(\omega) = \frac{(1 + A)\rho + C}{1 - B\rho}, \quad (4)$$

where parameters A , B , and C are determined by calibration against known reference standards. The method is similar to the three-way calibrations (open/short/50-ohm) used in the microwave impedance measurement with the terminations replaced by dielectric reference liquids, which more closely match the sensor response.

C. Instrumentation

Signals are acquired with an Agilent 54750 TDR oscilloscope with a 54754A differential plug-in, which has a 35-ps internal voltage step and a 20-GHz detection bandwidth. Reflected signals are captured nonuniformly on increasing time segments starting at 20 ps/cm and increasing to 500 μ s/cm. Laplace transforms are calculated numerically over all time segments¹⁹ with the last segment extrapolated to infinity and the final contribution calculated analytically. The incident pulse is recorded at the beginning of the sequence and used as a drift correction for all the later time segments. A vertical correction is applied to remove dc offsets between segments due to electrochemical effects.

Multiple sensors are monitored in succession using an HP87206B 6-port coaxial switch integrated with software control. The system can be integrated with low-frequency measurements under identical conditions by connecting both instruments to a common cure sensor through a coaxial switch. The four-wire output of an HP4192 impedance analyzer is converted to a coaxial configuration using an HP16095A impedance transformer allowing combined measurements over the frequency range of 10 Hz–10 GHz.

D. Sensors

Capacitance sensors must be physically small because the wavelength at highest frequencies is in the order of millimeters. At 10 GHz, the free-space wavelength is 30 mm, which reduces to 3–4 mm in high-permittivity aqueous solutions ($\lambda/\sqrt{\varepsilon}$, $\varepsilon=78$). The result is a quarter wavelength of 1 mm or less and care must be taken to avoid a quarter-wave resonance in the free-water relaxation.

The sensor used is a 3.6-mm-diameter semirigid coaxial line (Micro-Coax UT-141) with a short section of inner conductor protruding at its tip. The tip is formed by removing the outer conductor with a stripping tool (Huber-Suhner 74Z-0-0-157) and removing the Teflon sleeve with a razor blade. The tip is trimmed to between 0.5 and 1.5 mm with a rotary

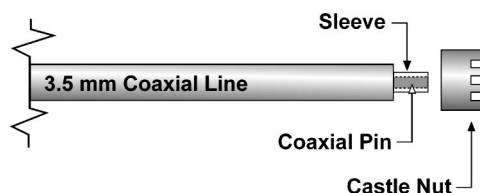


FIG. 1. Schematic of cement sensor.

tool as estimated under a microscope with the actual length determined by calibration. A diagram of the sensor is shown in Fig. 1.

Since the exposed tip is an effective radiator in high-permittivity liquids, it must be shielded to prevent radiation and distortion of the reflected signal. This is done by covering the tip with a serrated sleeve, which provides a surrounding ground plane while allowing a free flow of material through the tip. A 4.0×0.7 -mm castle nut²³ works well for this purpose; the nut is reamed with a 3.58-mm (0.141") drill and twisted onto the coaxial line with the serrations aligned with the sensor tip.

Prior to attaching the castle nut, the tip diameter is increased from 0.9 to 1.6 mm to maintain an approximate 50- Ω impedance. A 1.59-mm (0.125") slot pin is slid over the protruding conductor and ground to length with the rotary tool. To reduce electrochemical effects, both the slot pin and castle nut are sputtered with a gold/palladium alloy prior to an assembly. Reducing the electrochemical capacitance reduces the total RC decay in the reflected transient, improving transform stability and reducing sampling time.

E. Procedures

Measurements are performed differentially relative to the empty sensor, keeping the reflection coefficient large and closely approximating the permittivity at all but the highest frequencies. The calibration traces are taken with liquids of known permittivity and the sensor capacitance adjusted so that all display the correct permittivity. The capacitance values are typically in the range of 50–120 fF corresponding to pin lengths between 0.75 and 1.8 mm. Additional calibration traces are taken using saline solutions of varying molarity to approximate signals at early cure without the bound-water signal. By comparing the cement and saline reference signals, artifacts originating in the instrument and connecting lines can be removed.

The sample is placed in a sealed vial with the sensor line extending through a rubber septum in the cap. The samples are placed in a temperature-controlled water bath set to either 23 or 30 °C with thermocouples recording the temperature. Data is acquired every 10–15 min initially, then slowed to periods of hours after several days of cure. The acquisition is PC automated, with all data records, calibration records, temperature, and time stamp stored in a common data file for later analysis. A typical cure run records 2–300 individual records as a function of cure time, so monitoring is essentially continuous.

The real permittivity is verified to around 8 GHz using a bilinear calibration.¹⁸ The calibration records for acetonitrile ($\varepsilon'=37.5$) and dichloromethane ($\varepsilon'=8.85$) are used for lim-

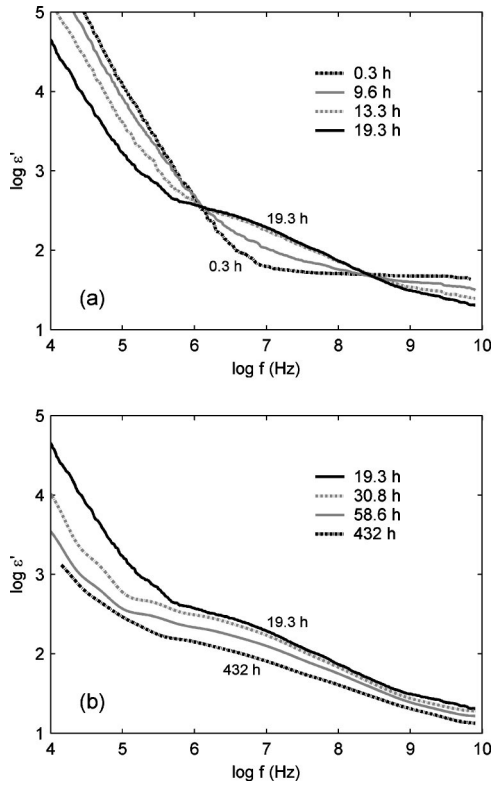


FIG. 2. Frequency dependence of the real permittivity during OPC cure ($w/c=0.4$, 23°C).

iting high- and low-permittivity references during the cure process. The bilinear coefficients A and B are generated for these references to produce a flat response for all the references over the range near 10 GHz. The same coefficients are then used to correct the permittivity for all the cement records with the coefficient C adjusted to align the differential and bilinear calibrations in the low-frequency limit. Since the bilinear calibration cannot be used at low frequencies where reference signals overlap, a crossover frequency around 1 GHz is chosen between the differential and bilinear displays.

III. FREQUENCY-DOMAIN BEHAVIOR IN OPC

A. Real permittivity

We begin with the basic changes in the complex permittivity and impedance, which occur as a function of cure time. Figure 2 shows the real permittivity ϵ' during the cure process over the frequency range of 10 kHz–8 GHz. The sample is monitored continuously from 0 to 430 h with the temperature held at 23°C throughout the sequence. The sequence begins immediately after mixing in Fig. 2(a), where the permittivity shows a broad-flat region above 10^7 Hz due to a free-water response and a large increase below 10^7 Hz due to an electrode polarization. The free-water permittivity is around 45, which is reduced from the pure value of 78 proportional to the volume of water (55%) in the cement paste. The permittivity shows a slight decrease around 8 GHz in accordance with the expected relaxation of free water.²⁴ The noise artifacts occurring around 10 MHz have been removed by calibration with the saline reference.

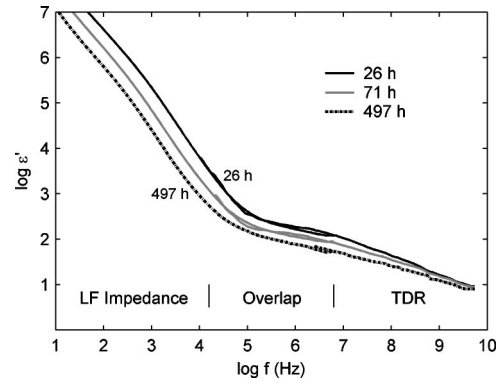


FIG. 3. Wide-range frequency dependence of the real permittivity during long-time OPC cure, using the combined TDR and low-frequency measurement ($w/c=0.4$, 23°C).

During the cure process, the high-frequency permittivity near 8 GHz decreases as free water is consumed in the reaction. The low-frequency permittivity below 1 MHz also decreases as the ion conductivity decreases, reducing polarization at the electrodes. Simultaneously, an intermediate-frequency signal begins to appear around 10 MHz, which is distinct from either the free-water relaxation or ion conductivity. The intermediate signal continues to grow for about 20 h, reaching a maximum permittivity around 300 as seen in Fig. 2(a). The intermediate signal then decreases and broadens with further cure time, as seen in the continuing sequence in Fig. 2(a). The slow decrease continues over periods of hundred of hours, extending into a range accessible to low-frequency instrumentation. This is verified by a combined TDR/low-frequency measurement in Fig. 3, in which a common TDR sensor is sampled by both instruments over the range of 10 Hz–8 GHz under identical conditions.

The intermediate-frequency signal is of particular interest because it cannot be accounted for by either the free-water relaxation or ion conductivity. It is not present in the initial cement paste but only appears after several hours of cure with a distinct frequency dependence. It apparently represents some additional relaxation forming with developing microstructure, and thus monitoring the formation of this microstructure. The signal increases at early cure as the microstructure develops and then decreases and broadens at longer times as the initial state becomes more tightly bound in the C–S–H gel.

B. Imaginary permittivity

The imaginary counterpart to Fig. 2 is dominated by ion conductivity, which produces a characteristic ω^{-1} variation over the frequency range. The imaginary component ϵ'' of each relaxation appears as a deviation from this ω^{-1} variation, making it easier to multiply by ω and display the dielectric conductivity directly. The imaginary component of each relaxation thus appears as a deviation from the horizontal base line.

Figure 4 shows the dielectric conductivity $\omega\epsilon''$ over the range of 10 kHz–3 GHz associated with Fig. 2. In the freshly mixed paste, the conductivity is dominated by a large flat base line across the frequency range representing a dc

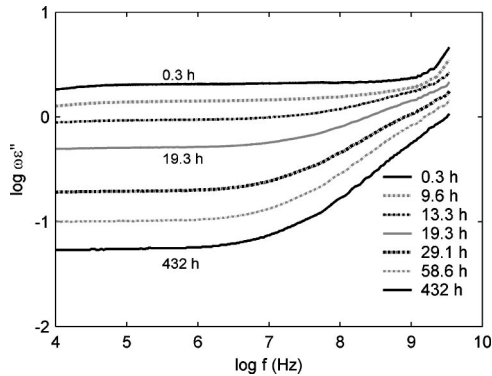


FIG. 4. Frequency dependence of the dielectric conductivity $\omega\epsilon''$ during OPC cure, corresponding to the real permittivity in Fig. 2 ($w/c=0.4$, 23°C).

conductivity. A small upturn above 1 GHz represents a free-water relaxation, where as a small roll off near 10 kHz represents an electrode polarization. As cure proceeds, the conductivity decreases as seen by the decreasing base line and an intermediate-frequency signal begins to appear as a deviation from the base line above 1 MHz. The deviation continues to grow with an advancing cure at each of the cure times corresponding to Fig. 2.

Both the real and imaginary behavior is in accord with other results in overlapping frequency ranges. Camp and Billota²⁵ report low-frequency measurements as a function of cure time at frequencies up to 7 MHz, showing a large polarization and ion conductivity that decreases with cure time. Dispersion in the range of 10^5 – 10^6 Hz is noted, which appears to be moving toward lower frequencies with an advancing cure. Van Beek¹⁴ shows a large permittivity dispersion between 1 and 1000 MHz, which increases with an initial cure and decreases thereafter. A decreasing ion-conduction base line is also seen with a growing deviation from a flat conductivity above 1 MHz. Ford *et al.*²⁶ show a permittivity plateau in the range of 10^4 – 10^7 Hz at 20 h cure with a permittivity exceeding the expected values for the free water. Gu and Beaudoin²⁷ present linear frequency measurements in the range of 1–1500 MHz in mature cement pastes showing large increases in permittivity below 100 MHz.

Though the intermediate-frequency behavior in Fig. 4 may appear to be the imaginary counterpart of the intermediate-frequency behavior in Fig. 2, the frequency dependence is not the same. A model fit to the permittivity relaxation in Fig. 2 requires a relaxation frequency around 10 MHz, whereas a model fit to the conductivity relaxation in Fig. 4 requires a relaxation frequency around 100 MHz. It thus appears that a second intermediate-frequency relaxation is present, one which is small compared to the original relaxation but accentuated by the ω^{-1} dependence of the dielectric conductivity. The presence of the two intermediate-frequency relaxations in both the permittivity and loss will be discussed in the next section.

C. Complex impedance

The results can be displayed in the complex impedance plane using the relation $Z^* = 1/i\omega C_0 \epsilon^*$. Figure 5 shows the

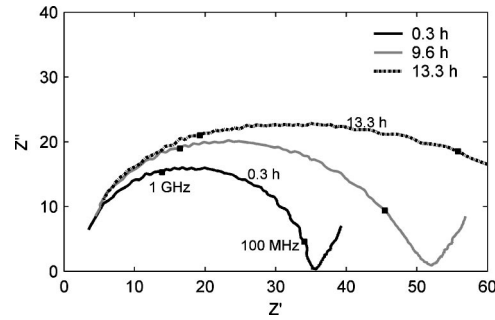


FIG. 5. Complex impedance during an early OPC cure, corresponding to the real permittivity in Fig. 2 and the dielectric conductivity in Fig. 4 ($w/c=0.4$, 23°C).

permittivity and conductivity at early cure, transformed to complex impedance over the range of 100 kHz–3 GHz. The figure shows the usual arc in the complex impedance plane representing an electrolyte resistance in parallel with an electrode capacitance. The arc is similar to the results in the literature^{28–32} except the electrolyte resistance is small and the RC time constant shifted into the gigahertz frequency range. We thus obtain the complex impedance at earlier cure times than the literature, where the RC time constants are large and the measurement is restricted to long cure times. We can also compare with the 100-MHz measurements of McCarter, where time constants are intermediate and the measurement is restricted to 1 day cure times.¹⁷

IV. FREQUENCY-DOMAIN MODELING IN OPC

A. Model description

The combined permittivity and conductivity are now fit to a dielectric model, which includes a broad relaxation around 1 MHz, a narrow relaxation around 100 MHz, a free relaxation around 20 GHz, and terms representing an ion conductivity and electrode polarization. The data is fit continuously to all five processes over the entire frequency range with the vertical weighted logarithmically to compensate for the large electrode polarization. The real and imaginary components are fit simultaneously using shared parameters, yielding a better convergence and providing the best overall fit between the real and imaginary components. The complex fitting is performed by laminating n real and imaginary points into an array of $2n$ elements long and using a conditional fit function defined as the real part for the first n elements and an imaginary part for the second n elements.

The large permittivity relaxation occurring around 1 MHz in Fig. 2 is assumed to follow a Cole-Davidson relaxation with an adjustable distribution parameter. This is in accordance with a variety of results in the literature including cement,¹² biopolymers,^{33,34} and other bound-water systems.³⁵ The contribution for this relaxation, which we designate the low relaxation, is written as

$$\epsilon(\omega) - \epsilon_\infty = \frac{C_l}{(1 + i\omega\tau_l)^\beta}, \tag{5}$$

where C_l is the low-relaxation amplitude, τ_l is the low-relaxation time, and β is the low-relaxation distribution parameter.

The conductivity relaxation occurring around 100 MHz in Fig. 4 is assumed to follow a Debye relaxation with no distribution parameter ($\beta=1$). This is consistent with the literature results that show near Debye-like behavior for bound water in clays.³⁶ Though some literature suggests a Cole-Cole relaxation with a variable distribution parameter, we choose a simple Debye term of first order to minimize the number of fitting variables. The contribution for this relaxation, which we designate the medium relaxation, is written as

$$\varepsilon(\omega) - \varepsilon_\infty = \frac{C_m}{1 + i\omega\tau_m}, \quad (6)$$

where C_m is the medium-relaxation amplitude and τ_m is the medium-relaxation time.

The free-water relaxation occurring at the highest frequencies is assumed to follow a Debye relaxation with a relaxation time of 8.2×10^{-12} ps.¹⁸ The distribution parameter is again set to unity consistent with a variety of results in the literature.³⁵ The contribution of this relaxation, which we designate the high or free relaxation, is similar to Eq. (6) with a free-relaxation amplitude C_f and relaxation time $\tau_f = 8.2 \times 10^{-12}$ ps. With the relaxation time fixed, the fit defaults to an adjustable additive constant at low frequencies.

Electrode polarization appearing at low frequencies is assumed to add a power-law term $C_p\omega^\gamma$ to the real part of the complex fit function. The ion conductivity appearing across a broad frequency range is assumed to add a constant term C_i to the imaginary part of the complex fit function. Adding all the terms together gives a combined complex fit function,

$$\begin{aligned} & \text{Re} \left[\frac{C_l}{(1 + i\omega\tau_l)^\beta} \right] + \text{Re} \left[\frac{C_m}{1 + i\omega\tau_m} \right] + \text{Re} \left[\frac{C_f}{1 + i\omega\tau_f} \right] \\ & + C_p\omega^\gamma \text{ (permittivity),} \\ & - \text{Im} \left[\frac{C_l}{(1 + i\omega\tau_l)^\beta} \right] \varepsilon_o\omega - \text{Im} \left[\frac{C_m}{1 + i\omega\tau_m} \right] \varepsilon_o\omega \\ & - \text{Im} \left[\frac{C_f}{1 + i\omega\tau_f} \right] \varepsilon_o\omega + C_i \text{ (conductivity),} \end{aligned} \quad (7)$$

where the nine fitting parameters are the low-relaxation time τ_l , the low-relaxation distribution parameter β , the medium-relaxation time τ_m , the polarization exponent γ , and the five amplitude factors C_l , C_m , C_f , C_p , and C_i . An additional power-law term can be added to the imaginary part of the complex fit function to correct for polarization in the conductivity at low frequencies. This requires two additional variables however and is generally avoided by setting the frequency limit for the conductivity fit higher.

B. Individual modeling

Individual modeling at specific cure times uses a two-stage process to minimize the number of fit variables at one time. During the first stage, the medium relaxation is eliminated and the remaining function fit over the frequency range of 10 kHz–8 GHz for the permittivity and 100 kHz–3 GHz for the conductivity. During the second stage, the polarization exponent γ is fixed and the remaining function fit above

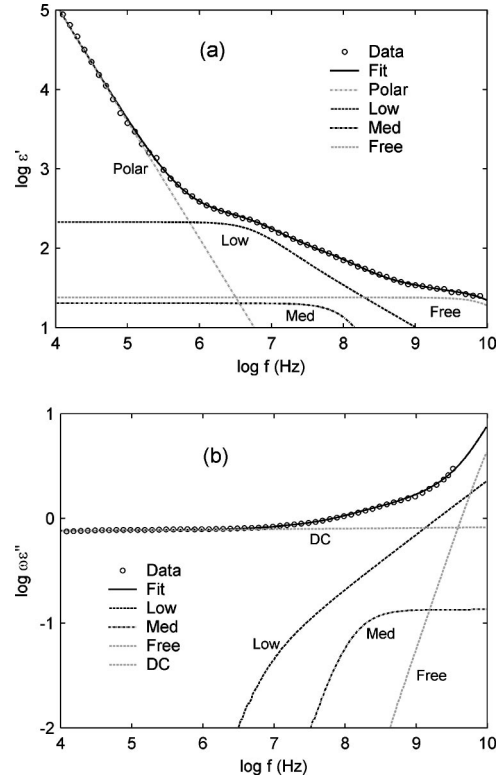


FIG. 6. Representative model fit for OPC at 15-h cure, showing the individual model components along with combined fit. The real permittivity and dielectric conductivity are fit using shared parameters ($w/c=0.4$, 23°C).

1 MHz with the medium relaxation included. The output values from the first fit are used as the input values for the second with the variance decreasing in an order of magnitude between the first and second fits. The process provides an approximate solution for the polarization below 1 MHz for the purpose of estimating the residual contribution above 1 MHz. It provides good resolution for both the low and medium relaxations.

Attention must be given to timing errors between the reference and unknown transients, which cause unwanted permittivity roll offs near 10 GHz and distort the free-water contribution. Errors as small as 1 ps can cause significant roll offs, particularly at early cure, where the free-water concentration is high. Such errors can propagate further into the model causing errors in the low-relaxation amplitude and distribution parameter. These errors are corrected by measuring the delay Δt between leading edges in the time domain and inserting the appropriate correction term $e^{j\omega\Delta t}$ in the frequency domain.

A typical model fit for OPC is shown in Fig. 6 at 15-h cure. For the permittivity, the model replicates the electrode polarization below 1 MHz, the low relaxation from 1 MHz to 1 GHz, and the free relaxation above 1 GHz. The fit is superimposed on the measured data along with the individual contributions for polarization, low relaxation, medium relaxation, and free relaxation. For the conductivity, the model replicates the conducting base line below 10 MHz along with the upturn above 10 MHz due to the low, medium, and free relaxations. The fit is again superimposed on

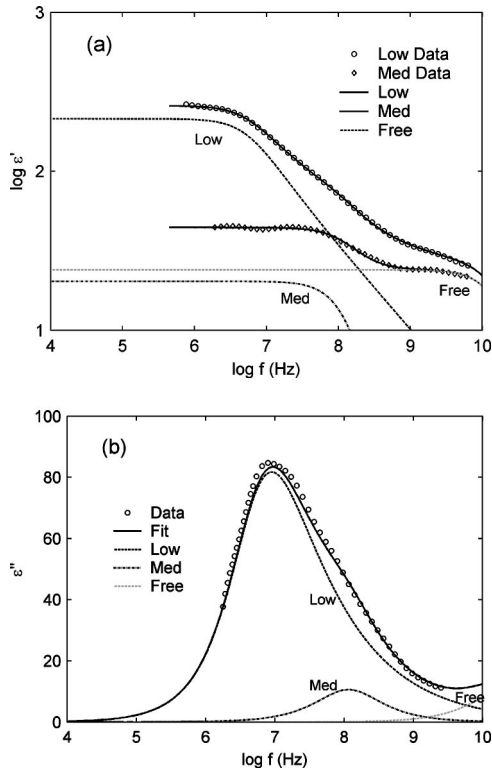


FIG. 7. Subtracted model fit for OPC at 15-h cure, showing the low- and medium-relaxation components for the real permittivity, and the combined low- and medium-relaxation fit for the imaginary permittivity ($w/c=0.4$, 23°C).

the measured data along with the individual contributions, and it is clear that the medium relaxation is required to replicate the conductivity behavior.

To ensure that both the low and medium relaxations are present with both the real and imaginary components, portions of the model fit are subtracted from the measured data and the remaining signal is enlarged. Figure 7 shows the measured permittivity with the polarization fit subtracted, showing an obvious permittivity transition for the low relaxation. The figure also shows the measured permittivity with both the polarization and low-relaxation fits subtracted, revealing a clear permittivity transition for the medium relaxation. For the conductivity, Fig. 7 shows the measured conductivity with the ion conductivity subtracted and displayed as dielectric loss by dividing by ω . The result shows a loss peak, which is a superposition of two loss peaks, each corresponding to the imaginary counterpart of the low and medium relaxations. As expected, the medium relaxation is about an order of magnitude smaller for both permittivity and loss.

C. Continuous cure modeling

The model is now fit to the changing permittivity spectrum continuously during the cure process, with the model parameters extracted as a function of cure time. All the nine model outputs are monitored as a function of cure time along with timing delay and variance, to identify obvious trends and anomalies. To reduce a point-to-point jitter in the polarization, a trendline is applied to the polarization exponents

and the model refit a second time using the trendline exponents to obtain new values for the polarization amplitude. The result is a polarization exponent and amplitude that varies smoothly with cure time and represents a time-averaged estimate of the residual polarization contribution above 1 MHz.

Procedures are as follows: starting at low frequencies, the model is fit to approximately 100 records with the medium relaxation disabled. A logarithmic trendline is applied to the exponent values and the model refit a second time using the trendline exponents with the medium relaxation enabled. The polarization parameters now vary smoothly with cure time and are immune to low-frequency noise appearing at long cure times. Continuing to high frequencies, the free-relaxation amplitude is monitored as a function of cure time with the timing errors corrected within the limits of the instrument resolution. Parameters representing both spectrum end points are now isolated from the problem and vary smoothly with cure time, including the polarization exponent, polarization amplitude, free-relaxation amplitude, and ion conductivity.

Of the five remaining parameters in the spectrum interior, the low-relaxation frequency and distribution parameter converge well, whereas the low-relaxation amplitude, medium-relaxation amplitude, and medium-relaxation frequency show some point-to-point interaction. A third fit is thus performed with the polarization parameters fixed and the fitting interval restricted above 1 MHz. The model now converges on all the nine parameters with only a slight interaction between the low- and medium-relaxation amplitudes. The fit can be further improved by eliminating an interval around 100 MHz from the fitting routine, which contains a small quarter-wave resonance in the input line.

D. Model results

The results of the modeling from 0 to 60 h are shown in Fig. 8. The free-relaxation amplitude begins at around 43, corresponding to the volume reduction of water to cement in the initial cement paste. The amplitude decreases with cure time showing a rapid decrease during the first 20 h and a more gradual decrease thereafter. The amplitude continues to decrease throughout the period, reaching a value around 8 at 60 h.

The low-relaxation amplitude begins at zero and rises to an effective permittivity near 300 at 20 h. It then decreases slowly with cure time for all times thereafter. The low-relaxation frequency decreases between 15 and 40 h, consistent with the decrease in Fig. 2, and shows a frequency around 7 MHz at 15 h and 3 MHz at 40 h. The low-relaxation distribution parameter also decreases with cure time, consistent with Fig. 2, and shows a distribution parameter around 0.55 at 15 h and 0.4 at 60 h. No low-relaxation data is available at less than 15 h as the low-relaxation behavior has not fully developed.

The medium-relaxation amplitude begins at zero and rises to an effective permittivity near 30 at 20 h. It shows a slightly faster onset and an earlier peak time than the low-relaxation amplitude. As with the low relaxation, it decreases

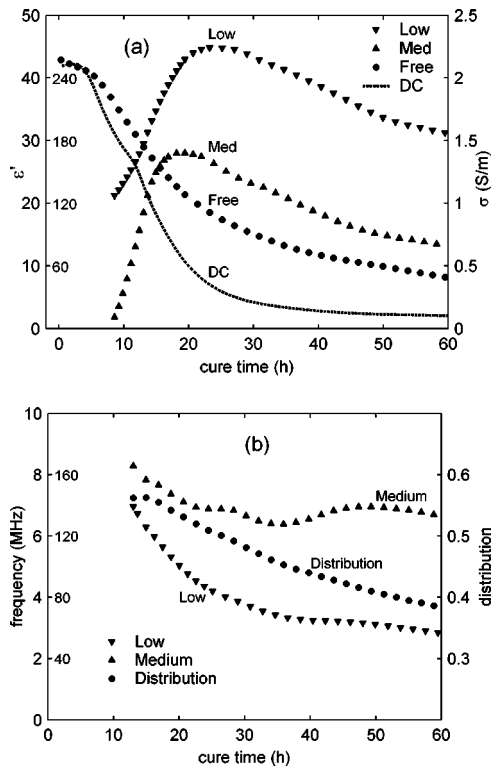


FIG. 8. Evolution of model parameters during OPC cure, showing the relaxation amplitudes, frequencies, and distributions factors as a function of cure time ($w/c=0.4$, 23°C).

with an increasing cure time for all times thereafter. The medium-relaxation frequency is relatively constant through the period, varying between approximately 130 and 150 MHz. The conductivity amplitude decreases from 2 to 0.1 S/m during the period, in accordance with other low-frequency results.

The model shows obvious similarities with Miura *et al.*¹² who performed the TDR measurements on cement paste at 1 h and 57 days. The authors report a ~ 100 -MHz relaxation appearing at 1 h with an amplitude well below the free relaxation at that point. They also report a ~ 1 -MHz relaxation appearing at 57 days with an amplitude comparable to the free-relaxation at the beginning. They also report the free-relaxation amplitude dropping to relatively low values less than 5 during the period. The authors attribute the 100-MHz relaxation to water that is attached to the calcium silicate through hydrogen bonds and the 1-MHz relaxation to water that is attached to the calcium silicate by chemical bonds. The 100- and 1-MHz relaxations appearing at 1 h and 57 days seem to correspond to our medium and low relaxations, which we follow throughout the cure process. The low value for the free-relaxation amplitude at long cure times appears to correspond to our low values in Fig. 8. Small differences could be attributed to Miura *et al.* using a surface-contact probe, with our measurements using an internal sensor.

The model also shows similarities with Hafiane *et al.*¹³ who performed the noncontact rf measurements on cement disks between 1 MHz and 1.8 GHz. The authors report relaxations at 22 MHz for cure times of 10 h and around 1 MHz for cure times between 14 and 18 h. They also at-

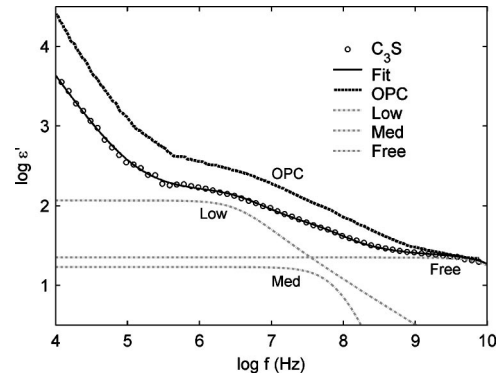


FIG. 9. Representative model fit for the C_3S paste at 21-h cure, showing the individual model components along with combined fit ($w/c=0.4$, 23°C). The OPC model fit at 21 h overlaid for comparison.

tribute these features to the relaxations of water that is either hydrogen bonded or incorporated into hydrates.

V. FREQUENCY-DOMAIN BEHAVIOR IN TRICALCIUM SILICATE

A. Tricalcium silicate

The origins of the low and medium relaxations are explored by comparing the permittivity evolution in OPC with tricalcium silicate paste. The amplitude evolution in C_3S is similar, showing a decrease in the free relaxation and an appearance of the low and medium relaxations. The frequency evolution is also similar, decreasing from 6 to 4 MHz for the low relaxation and remaining constant around 90 MHz for the medium relaxation. The distribution parameter is higher, decreasing from around 0.7 to 0.55 for the low relaxation. However, the magnitude of the low-relaxation amplitude is significantly smaller, showing only about a third of the amplitude in OPC.

Figure 9 shows a comparison of the C_3S and OPC permittivity at 21 h showing a similar free relaxation around 5 GHz and a significantly smaller low relaxation around 1 MHz. The model relaxations are superimposed in the diagram, showing the low, medium, and free relaxations as well as the combined fit. The model evolution with cure time is similar to Fig. 8, with the low-relaxation amplitude reaching a maximum around 120 for C_3S versus 280 for OPC. The conductivity is also smaller because of the lower ion concentration, decreasing from 0.5 to 0.03 S/m during the period versus 2.0–0.1 S/m for OPC. The free-relaxation amplitude is larger at long cure times, appearing around 20 at 50-h cure versus 10 for OPC.

Measurements have been made in a “simulated” cement consisting of the tricalcium silicate, tricalcium aluminate, and gypsum, mixed in a ratio of 77.8/14.5/7.8 wt % and hydrated at $w/c=0.4$. The signal evolution is similar to the pure C_3S , which is expected as the simulated cement contains 78% C_3S by weight.

B. Tricalcium silicate with added potassium sulfate

The low relaxation in the C_3S paste is significantly affected by an increasing ion concentration. Two C_3S samples are prepared with $w/c=0.4$ and cured under identical condi-

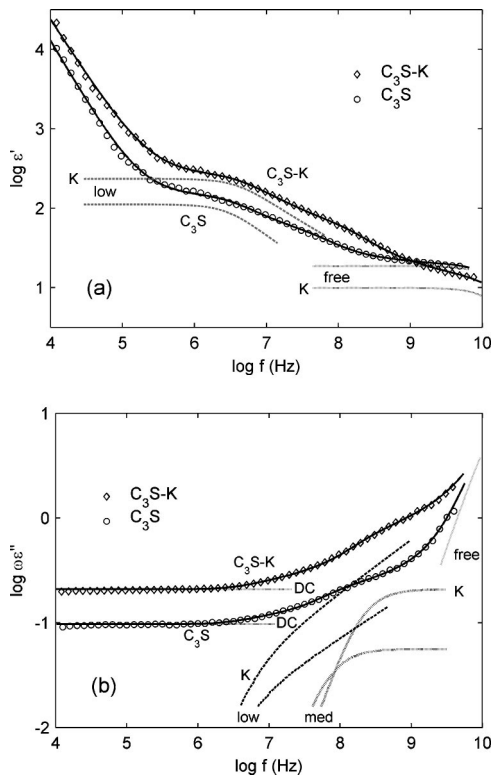


FIG. 10. Effect of ionic strength on the C_3S paste at 19-h cure, showing the individual model components along with the combined fit for both samples ($w/c=0.4$, $23^\circ C$).

tions with one containing pure water and the other a 0.3 M solution of potassium sulfate. As expected, the paste with potassium sulfate shows a higher conductivity and electrode polarization but also a larger low-relaxation amplitude. This increase is shown in Fig. 10 at 20 h and is similar to the increase between the C_3S and OPC in Fig. 9. The free-relaxation amplitude is slightly lower in the potassium sulfate paste as expected in the ion-containing solutions.^{37,38}

The specific nature of this variation is shown by the model fit and subtraction, as seen in Fig. 11. For the permittivity, the low relaxation is formed by taking the measured permittivity and subtracting the model fits for polarization, medium relaxation, and free relaxation. The medium relaxation is similarly formed by taking the measured permittivity and subtracting the model fits for polarization, low relaxation, and free relaxation. For the loss, the combined relaxation is formed by taking the measured conductivity and subtracting the model fit for ion conductivity and then dividing by ω . The differences are displayed along with the model fits for the low, medium, and free relaxations.

From the model fit, the low-relaxation amplitude for the potassium sulfate sample is over twice as large as the straight cement paste ($\epsilon' = 235$ versus 112). The medium-relaxation amplitude, however, shows a much smaller increase between the two cement pastes ($\epsilon' = 19.8$ versus 15.3). The free-relaxation amplitude is lower for the potassium sulfate sample ($\epsilon' = 9.9$ versus 18.7), similar to the OPC, whereas the dc conductivity is higher for the potassium sulfate sample (0.21 S/m versus 0.07 S/m).

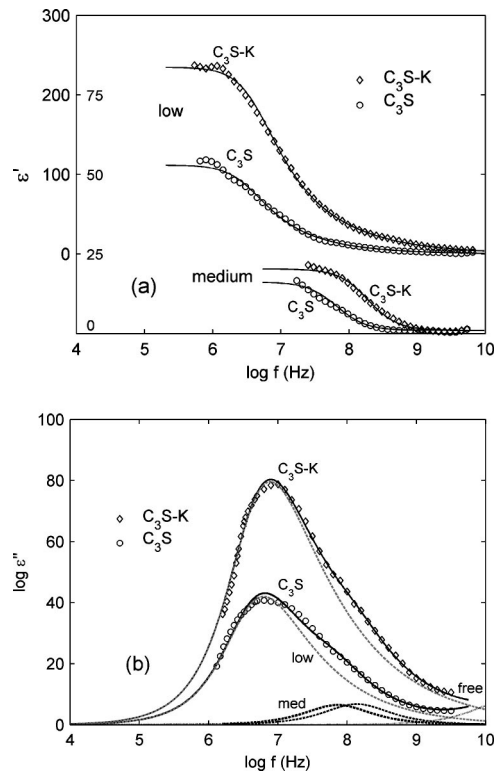


FIG. 11. Effect of ionic strength on the C_3S paste at 19-h cure, showing the subtracted low- and medium-relaxation components for real permittivity and the combined low- and medium-relaxation fit for imaginary permittivity for both samples ($w/c=0.4$, $23^\circ C$).

The potassium sulfate measurements provide insight into the source of the low and medium relaxations. The low relaxation is enhanced by a higher ion concentration, either in the C_3S with added potassium ions or in comparison with OPC. The low relaxation is nevertheless distinct from the bulk ion conduction because its frequency dependence follows a Cole-Davidson relaxation rather than a dc conduction model. The medium relaxation, on the other hand, shows a much smaller difference with the ion concentration, either in the C_3S with potassium sulfate or in comparison with OPC.

Two possible sources are suggested for this behavior. The first is a bulk polarization model suggested by McCarter *et al.*^{39,40} in which double-layer processes operating on the gel surface increase the polarizability of the paste, thus increasing the permittivity in a frequency range above the electrode polarization. The permittivity increases with the initial outgrowth of the hydration products forming on the grain surfaces and then decreases with the infilling of pore space by the hydration products that decrease the surface area. The resulting signal is distinct from the ion conduction, which shows no frequency variation as well as the electrode polarization that only appears at lower frequencies. The model accounts for a low-relaxation amplitude higher than the permittivity of free water and accounts for the increased signal amplitude with higher ion concentration, where more ions are available for the gel surfaces.

The second possible source is a bound-water model suggested by van Beek¹⁴ in which water binds to developing microstructure and takes on a relaxation distinct from bulk water. Decreases in frequency and amplitude occur with cure

time as loosely bound layers of adsorbed water become more tightly bound. Thick layers of pore water with outer layers having a high relaxation frequency become thin layers of pore water with the remaining layers having a low relaxation frequency. The bound-water amplitude increases and during an early cure as the free-water amplitude decreases, reflecting a conversion of unreacted water to adsorbed water. The model accounts for a medium-relaxation amplitude less than the permittivity of free water and is consistent in frequency with a variety of bound-water behavior in clays,³⁶ biological systems,^{33,34} and other systems.⁴¹

Considering both relaxations, we speculate that the low relaxation represents the bulk polarization similar to the McCarter model, whereas the medium relaxation represents the bound water similar to the van Beek model. The low relaxation is produced by ions accumulating on the gel surface and is more directly affected by ion content. The medium relaxation is produced by layers of adsorbed water accumulating on the pore surface and is less affected by ion content. Regardless of the mechanism involved, the two relaxations represent the charged species accumulating in some manner on developing microstructure, and thus monitoring the formation of this microstructure.

VI. CONSTANT-FREQUENCY AND TRANSIENT RESPONSE

A. Constant-frequency evolution

Extracting the permittivity at selected frequencies as a function of cure time allows comparison with single-frequency measurements in the literature. Figure 12 shows the single-frequency permittivity obtained from Fig. 2; similar analysis can be done with the conductivity in Fig. 4. Frequency slices at 1 and 5 GHz are shown in Fig. 12(a) and compared with the free-relaxation amplitude, whereas slices at 10, 50, and 200 MHz are shown in Fig. 12(b) and compared with the low-relaxation amplitude. Overlaid on the frequency slices are model-predicted slices obtained by calculating the model amplitude using the parameters in Fig. 8 and evaluating at the specific frequencies. The predicted amplitudes agree well and confirm the consistency of the model.

The 1- and 5-GHz amplitudes approximate the free-relaxation amplitude, starting at around 40 and decreasing with cure time. The 5-GHz amplitude is smaller because it represents a decreasing portion of the free-relaxation spectrum. Both amplitudes are larger than the free-relaxation amplitude because they include a high-frequency contribution from the stretched low relaxation. The 5-GHz amplitude shows a decrease with cure time similar to 9.5-GHz waveguide measurements by Ding *et al.*¹⁶

The 10- and 50-MHz slices approximate the low-relaxation amplitude, increasing with cure time initially and then decreasing after about 20 h. Both amplitudes are smaller than the low-relaxation amplitude because they represent a decreasing portion of the low-relaxation spectrum. The 200-MHz slice is even smaller because it represents a transition between the high- and low-frequency extremes. The 10- and 50-MHz amplitudes show a variation with cure time similar to the 20-MHz measurements by van Beek¹⁴ and

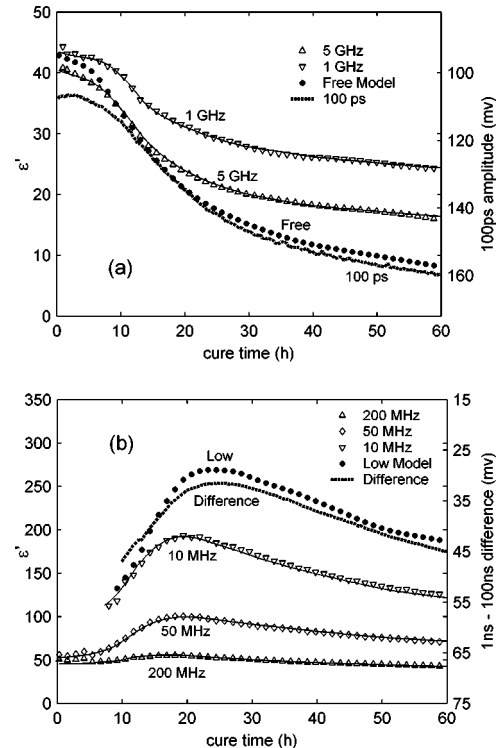


FIG. 12. Constant-frequency permittivities during OPC cure as extracted from Fig. 2. Permittivities at 1 and 5 GHz compared to the free-relaxation model and permittivities at 10, 50, and 200 MHz compared to the low-relaxation model, with model-predicted permittivities overlaid on measured values. The 100-ps transient amplitude and (1–100 ns) difference signal overlaid for comparison ($w/c=0.4$, 23°C).

3-MHz measurements by Olp *et al.*¹⁵ Slices below 1 MHz show an initial electrode polarization similar to the 100-kHz measurements by McCarter *et al.*^{39,40}

B. Transient amplitude evolution

TDR offers an advantage over the frequency-domain methods in that rate-dependent behavior can be interpreted in either time or frequency domain. This can be important in the field implementation, where the amplitude of the reflected transient can be followed directly without a phase-sensitive frequency transform.

Figure 13 shows the reflected transient from which the frequency data is derived. The signal is captured on seven successive time scales, beginning at 20 ps/cm on the left and ending at 500 $\mu\text{s}/\text{cm}$ on the right. The transient is inverted in the usual manner, showing the empty-sensor reflection at the top and the two constant-permittivity reference liquids ($\epsilon'=21.1, 37.5$) below. The reference liquids show an exponential decay indicating a constant sensor capacitance in series with the 50- Ω line. Also shown is the cement paste, which shows a superexponential decay spanning many decades due to the varying sensor capacitance. At 1 h, the transient shows a large amplitude on the 20-ps/cm time scale, indicating a free-water activity, followed by a long base line on the later time scales indicating an ion conduction. At 20 h, the transient shows a smaller amplitude on the 20-ps/cm time scale, indicating a reduced free-water activity, followed by a continuing decay on the later time scales

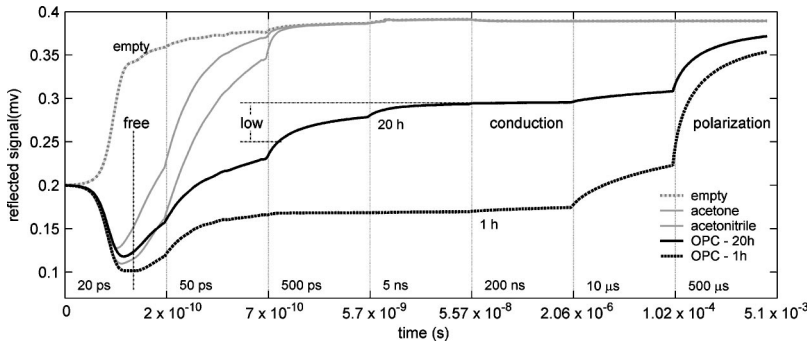


FIG. 13. Direct TDR transient captured on the nonuniform time scale, showing the empty-sensor and reference reflection ($\epsilon' = 21.1, 37.5$) along with the OPC reflection at 1 and 20-h cure. The location of the transient amplitudes identified for both the free- and low-relaxation indicators ($w/c=0.4, 23^\circ\text{C}$).

indicating additional relaxations. The conducting base line decreases with a decreasing ion conductivity.

A simple indicator for the free relaxation is the amplitude on the 20-ps/cm scale near the peak of the reflected signal. The delay time is approximately 100 ps, representing response in the gigahertz frequency range ($\omega = 1/t$). A simple indicator for the low relaxation is the amplitude on the 500-ps scale, where the reference transients have decayed to zero yet continuing cement decay is seen. The delay here is around 1 ns, representing response in the subgigahertz frequency range. To remove conductivity, the base line at 100 ns is subtracted, leaving a difference signal above the conductivity, which cannot be accounted for by the free-water relaxation. The resulting free- and low-relaxation indicators are superimposed in Fig. 12.

C. Hydration rate

The free- and low-relaxation indicators show the variation in the hydration rate with cure temperature. Figure 14 shows the evolution of both indicators for the two OPC pastes undergoing cure at different temperatures, one at 23.0°C ($\pm 0.5^\circ\text{C}$) and the other at 30.0°C . The 30°C sample shows a faster decay of the free-relaxation indicator as well as an earlier maximum of the low-relaxation indicator.

The free-relaxation indicator can be correlated with the exothermic heat of reaction as measured by calorimetry. This is shown in Fig. 14, where the degree of hydration is superimposed on the free-relaxation indicator, with the scaling and offset adjusted for convenience. The degree of hydration is

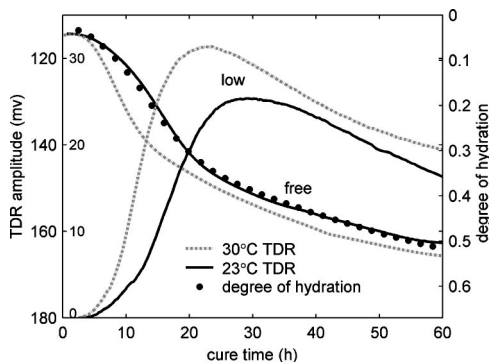


FIG. 14. Evolution of the free- and low-relaxation indicators during OPC cure for the two pastes cured at 23 and 30°C ($w/c=0.4$). Comparison of the free-relaxation indicator with the degree of hydration as measured by isothermal calorimetry.

obtained by an isothermal calorimetry, with the values normalized to the volumetric phase compositions of OPC (Ref. 20) and the known values of heat-of-hydration for the major phases in cement.²

VII. CONCLUSIONS

We have demonstrated a continuous monitoring of cement hydration using the time domain reflectometry with an embedded capacitance sensor. Measurements are made over a broad frequency range of 10 kHz–8 GHz from the initial mixing to several weeks of cure. The complex permittivity separates into three components: a low relaxation occurring near 1 MHz, a medium relaxation occurring at around 100 MHz, and a free relaxation occurring near 20 GHz. The evolving permittivity is modeled continuously during hydration, with the individual model parameters extracted as a function of cure time. The results are compared with other broadband measurements in overlapping frequency and cure states and with single-frequency measurements available in the literature. Measurements are extended to ranges accessible to low-frequency instrumentation and presented in a complex impedance form showing an expected arc behavior.

The source of the low relaxation is explored by comparing with tricalcium silicate paste and tricalcium silicate with varying ionic strength. The low relaxation is significantly reduced in C_3S compared to OPC but shows a similar amplitude when added salts are present. The medium relaxation is affected to a lesser extent, and we speculate that the low relaxation results from the bulk polarization of ions accumulating on the gel surface, whereas the medium relaxation represents water attaching to developing microstructure and acquiring a relaxation distinct from bulk water.

A simplified method is presented for analyzing the rate of reaction from the direct TDR transient. The method is demonstrated using a variation in temperature and a comparison with the exothermic heat of reaction. Since the transient indicators scale with the free-water concentration and microstructure formation, they can be used to follow variations in reaction rate with different cement formulations and cure conditions. They can also be integrated with a simplified TDR electronics package to form a robust cure-monitoring system usable in the field.

Future work will involve investigating variations in the cement formulation with differences in the relaxation behavior and cure evolution. The automation of fitting routines and computation reduction would greatly speed the analysis.

Both the frequency and transient analysis could be used to monitor variations in water-to-cement ratio, particle size distribution, addition of retarders and accelerants, and other additives.

ACKNOWLEDGEMENTS

The authors would like to acknowledge Dr. Vijay Gupta of Grace Performance Chemicals, who provided the calorimetry data in this work, and Dr. Edward Garboczi of NIST for the many helpful discussions. This work was supported in part by NSF Contract No. DMI-0128496.

- ¹Cement chemistry notation: C=CaO, S=SiO₂, H=H₂O, and A=Al₂O₃.
²H. F. W. Taylor, *Cement Chemistry*, 2nd ed. (Thomas Telford Publishing, London, 1997).
³M. Tarrida, M. Madon, B. L. Rolland, and P. Colombet, *Adv. Cem. Based Mater.* **2**, 15 (1995).
⁴I. G. Richardson, *Cem. Concr. Res.* **29**, 1131 (1999).
⁵J. J. Thomas, H. M. Jennings, and A. J. Allen, *Cem. Concr. Res.* **28**, 897 (1998).
⁶R. J. Wittebort, M. G. Usha, D. J. Ruben, D. E. Wemmer, and A. Pines, *J. Am. Chem. Soc.* **110**, 5668 (1988).
⁷R. Rassem, H. Zannithevenneau, D. Heidemann, and A. Grimmer, *Cem. Concr. Res.* **23**, 169 (1993).
⁸S. A. FitzGerald, D. A. Neumann, J. J. Rush, D. P. Bentz, and R. A. Livingston, *Chem. Mater.* **10**, 397 (1998).
⁹J. J. Thomas, S. A. FitzGerald, D. A. Neumann, and R. A. Livingston, *J. Am. Ceram. Soc.* **84**, 1811 (2001).
¹⁰D. Heidemann and W. Wieker, *Nuclear Magnetic Resonance Spectroscopy of Cement-Based Materials*, edited by P. Colombet (Springer-Verlag, Berlin, 1998), pp. 169–180.
¹¹D. Eisenberg and W. Kauzmann, *The Structure and Properties of Water*, (Oxford Press, London, 1969).
¹²N. Miura, N. Shinyashiki, S. Yagihara, and M. Shiotsubo, *J. Am. Ceram. Soc.* **81**, 213 (1998).
¹³Y. Hafiane, A. Smith, P. Abélard, J.-P. Bonnet, and P. Blanchart, *Ceramics-Silikáty* **43**, 48 (1999).
¹⁴A. van Beek, Ph.D. thesis, Delft University, 2000.
¹⁵K. Olp, G. Otto, W. C. Chew, and J. F. Young, *J. Mater. Sci.* **26**, 2978 (1991).
¹⁶X. Z. Ding, X. Zhang, C. K. Ong, B. T. G. Tan, and J. Yang, *J. Mater. Sci.* **31**, 5339 (1996).
¹⁷W. J. McCarter, S. Garvin, and N. Bouzid, *J. Mater. Sci. Lett.* **7**, 1056 (1988).
¹⁸R. H. Cole, J. G. Berberian, S. Mashimo, G. Chryssikos, A. Burns, and E. Tombari, *J. Appl. Phys.* **66**, 793 (1989).
¹⁹N. E. Hager III, *Rev. Sci. Instrum.* **65**, 887 (1994).
²⁰D. P. Bentz, X. Feng, C. J. Haecker, and P. E. Stutzman, NIST Internal Report No. 6545, 2000.
²¹D. P. Bentz, C. J. Haecker, X. P. Feng, and P. E. Stutzman, *Process Technology of Cement Manufacturing*, Fifth International VDZ Congress Proceedings (Düsseldorf, Germany, 2002), pp. 53–63.
²²Construction Technology Laboratories Inc., 5400 Orchard Lane, Skokie, Illinois.
²³Metric & Multistandard Components Corp., Hawthorne NY, Part #935.
²⁴M. Merabet and T. K. Bose, *J. Phys. Chem.* **92**, 6149 (1988).
²⁵P. R. Camp and S. Bilotta, *J. Appl. Phys.* **66**, 6007 (1989).
²⁶S. J. Ford, J. H. Hwang, J. D. Shane, R. A. Olson, G. M. Moss, H. M. Jennings, and T. O. Mason, *Adv. Cem. Based Mater.* **5**, 41 (1997).
²⁷P. Gu and J. J. Beaudoin, *Advances in Cement Research* **9**, 1 (1997).
²⁸W. J. McCarter, *Cem. Concr. Res.* **24**, 1097 (1994).
²⁹W. J. McCarter, G. Stars, and T. M. Chrisp, *Cem. Concr. Res.* **29**, 377 (1999).
³⁰M. Keddama, H. Takenouti, X. R. Nóvoa, C. Andrade, and C. Alonso, *Cem. Concr. Res.* **27**, 1191 (1997).
³¹R. T. Coverdale, B. J. Christensen, H. M. Jennings, T. O. Mason, D. P. Bentz, and E. J. Garboczi, *J. Mater. Sci.* **30**, 712 (1995).
³²C. Andrade, V. M. Blanco, A. Collazo, M. Keddama, X. R. Nóvoa, and H. Takenouti, *Electrochim. Acta* **44**, 4313 (1999).
³³N. Miura, N. Asaka, N. Shinyashiki, and S. Mashimo, *Biopolymers* **34**, 357 (1994).
³⁴N. Miura, Y. Hayashi, N. Shinyashiki, and S. Mashimo, *Biopolymers* **36**, 9 (1995).
³⁵T. Ishida and T. Makino, *J. Colloid Interface Sci.* **212**, 144 (1999).
³⁶T. Ishida, T. Makino, and C. Wang, *Clays Clay Miner.* **48**, 75 (2000).
³⁷P. Winsor and R. H. Cole, *J. Phys. Chem.* **86**, 2486 (1982).
³⁸R. Buchner, G. T. Hefter, and P. M. May, *J. Phys. Chem. A* **103**, 1 (1999).
³⁹W. J. McCarter, T. M. Chrisp, and G. Starrs, *Cem. Concr. Res.* **33**, 197 (2003).
⁴⁰W. J. McCarter, T. M. Chrisp, and G. Starrs, *Cem. Concr. Compos.* **21**, 277 (1999).
⁴¹U. Kaatz, *J. Mol. Liq.* **56**, 95 (1993).